Oceanologia 64 (2022) 457—472

Available online at www.sciencedirect.com

ScienceDirect

journal homepage: www.journals.elsevier.com/oceanologia

ORIGINAL RESEARCH ARTICLE

Numerical study of coastal wave profiles at the sandy beaches of Nowshahr (Southern Caspian Sea)

Seyed Masoud Mahmoudof*, Mohammadali Lotfi Takami

Iranian National Institute for Oceanography and Atmospheric Sciences (INIOAS), Tehran, Iran

Received 14 November 2021; accepted 9 March 2022
Available online 20 March 2022

KEYWORDS
SWASH Model;
Caspian Sea;
Wave evolution;
Infragravity waves;
Short wind-waves

Abstract This study aimed to investigate the capability of the one-dimensional (1D) mode of the Simulating WAves till SHore (SWASH), as a non-hydrostatic wave-flow model with six vertical layers, to reproduce the cross-shore wave evolution. For this purpose, the given model was initially calibrated for wave energy and the outputs were then verified with the field data measured at the Southern Caspian Sea. The calibration coefficients obtained for wave breaking are significantly less than the ones which have been mostly reported in previous studies for the two-dimensional (2D) mode of the SWASH. Although the reproduced wave height parameters are generally in good accordance with the field observations, the period parameters and the number of waves are overestimated and underestimated by the model, respectively. Moreover, the inaccuracies at the shallow stations are worse than at the transitional depths. The overestimation in both the reproduced energy of infragravity waves (IG) and their wavelength along with the underestimation in the wind-wave energy content are also among the factors responsible for the model deficiencies. The findings have revealed that the overestimation of the reproduced IG waves is the main reason for the underestimation of the breaking dissipation rate for irregular wave trains in the 1D mode. Therefore, more intensive breaking dissipation via selecting lower coefficient values is necessary to exhaust a certain energy content from longer waves in the 1D mode. This approach ultimately induces an over-dissipation of short wind-waves.
© 2022 Institute of Oceanology of the Polish Academy of Sciences. Production and hosting by Elsevier B.V. This is an open access article under the CC BY-NC-ND license (http://creativecommons.org/licenses/by-nc-nd/4.0/).

* Corresponding author at: Iranian National Institute for Oceanography and Atmospheric Sciences (INIOAS), Tehran, 1411813389, Iran.
E-mail address: m_mahmoudof@inio.ac.ir (S.M. Mahmoudof).
Peer review under the responsibility of the Institute of Oceanology of the Polish Academy of Sciences.

Production and hosting by Elsevier

https://doi.org/10.1016/j.oceano.2022.03.001
0078-3234/© 2022 Institute of Oceanology of the Polish Academy of Sciences. Production and hosting by Elsevier B.V. This is an open access article under the CC BY-NC-ND license (http://creativecommons.org/licenses/by-nc-nd/4.0/).

1. Introduction

Almost all nearshore hydrodynamic processes are controlled by wave transformations. Wind-waves, with periods lasting between 4 and 20 s, propagating toward shorelines also sense seabed disturbance, become skewed and asymmetric, and then break. The energy released from depth-induced wave breaking then drives nearshore currents, rips, and undertows and consequently causes sediment transport and morphological changes (Hoefel and Elgar, 2003; Longuet-Higgins and Stewart, 1964; Longuet-Higgins, 1970; MacMahan et al., 2006; Svendsen, 1984). Some energy content also transfers to low-frequency waves, known as infragravity (IG) waves or surf beat, having periods in the range of 20–200 s, and some other part transfers to higher harmonics through wave coupling or bore waves.

The IG waves, with small heights in deep water (Webb et al., 1991), may thus have the most energy contribution of the total wave train across inner surf and swash zones, especially under high-energy conditions (Gao, et al., 2019; Guza and Thornton, 1982). The domination of IG waves for stormy conditions in very shallow water also results in energy spectra with IG peaks, concurrent with flattening wind-wave peaks due to breaking dissipation. Numerous studies reported the stronger dependency of IG wave energy on swell than sea waves (e.g., Elgar et al., 1992; Mahmoudof, 2018a; Ruessink, 1998). Such waves can have significant impacts on dune erosion, sand bar, or mudflat formation (de Bakker et al., 2016a; de Vries et al., 2008; Roelvink et al., 2009), and may give rise to resonance and disorder in continuous dock operations in large harbors (Gao et al., 2020, 2021; González-Marco et al., 2008). The time-varying breakpoints of irregular waves during high-energy conditions and negative nonlinear wave-wave interactions under moderate conditions are known as two main generating sources of released and bound IG waves, respectively (Hasselmann, 1962; Longuet-Higgins and Stewart, 1962; Symonds et al., 1982). Battjes et al. (2004) realized the role of normalized bed slope parameter as $\beta_b = \frac{\alpha}{\omega}\sqrt{\frac{g}{d_b}}$ in the domination of each generating mechanism of IG waves. In this relationship, α is the bed slope, ω denotes the angular frequency, g, and d_b are the gravitational acceleration and the averaged breaking depth, respectively. In a mild-slope regime with $\beta_b < 0.3$, the generation of bound IG type as a result of nonlinear interactions is dominant. Larger values of β_b imply a steep-slope regime wherein the released type of IG due to moving breakpoints dominates in the surf zone. On very steep beaches or coastal cliffs, wherein IG waves are not fully dissipated, a significant proportion of their energy can thus reflect toward the sea, resulting in significant reflection coefficients close to or even greater than unity (Guza and Thornton, 1985; Mahmoudof et al., 2021; Sheremet et al., 2002). However, the energy of such waves is considerably dissipated until shorelines. The dissipation mechanisms of these waves have been thus far discussed in numerous studies (e.g., de Bakker et al. 2014; Ruju et al., 2012). On the other hand, positive triad wave-wave interaction is one of the processes that can transfer energy to higher harmonics in the shoaling zone. The primary swell waves can also decouple and decompose to several shorter and smaller secondary waves indicating a mild energy transfer to high-frequency harmonics especially on barred beaches (Masselink, 1998).

Considering the complexity of coastal hydrodynamic processes controlled by wave transformation, numerical models are useful tools to assess and predict these phenomena. Therefore, the models proposed for this purpose need to evaluate coastal wave evolution accurately. To meet this objective, wave characteristics and statistics (e.g., wave heights and period parameters) reproduced by such models must be verified with those observed in the field and laboratory measurements.

In this regard, phase-averaged or spectral wave models operate based on the energy-action equation, and solve the known source and sink terms (Komen et al., 1994; the Wave Model Development and Implementation Group [WAMDI], 1988). One of the important assumptions of these models is that the wave field is often founded on the near-Gaussian distribution, which is not valid in the shallow waters of nearshores due to the nonlinear effects of the wave field. The inaccuracy of phase-averaged models as a result of this discrepancy accordingly reveals the demand for models with the capability to capture high-order wave-wave interactions and reproduce wave nonlinearities near the shores.

Phase-resolving wave models can simulate the nonlinearities of shallow-water waves and reproduce nearshore hydrodynamic processes driven by wave transformations. Generally, the success of these models to represent coastal wave evolution has been thus far confirmed in several studies (e.g., Madsen et al., 2002; Torres-Freyermuth et al., 2007). The main concerning problem facing the application of these models is their high computational cost and time, even for small-scale domains. The Boussinesq and non-hydrostatic types of phase-resolving models are generally exploited to simulate coastal scale applications. The first type is a developed representation of weakly dispersive models (Gao, et al., 2017; Madsen et al., 2002; Nwogu, 1993; Wei et al., 1995). On the other hand, the non-hydrostatic models solve the basic conservation equations for mass and momentum (Ma et al., 2012; Stelling and Zijlema, 2003; Yamazaki et al., 2009). In the non-hydrostatic models, the free surface of the water is described using a single-valued function of the horizontal plane. However, these models often fail to accurately reproduce the details of wave-breaking processes such as air entrainment, wave-induced turbulence, and overturning.

The Simulating WAves till Shore (SWASH), as a non-hydrostatic wave-flow model based on nonlinear shallow water equations, is capable to explain complex changes in rapidly varying flows. The model assumes a hydrostatic pressure approximation in the frontline of breaking waves, ensuring that the waves develop a vertical face. The SWASH is also known as a valuable tool to investigate coastal wave processes controlled by wave breaking, such as frequency energy transfer, cease of wave-wave coupling, as well as IG wave generation and dissipation. Thus, an accurate evaluation of coastal wave breaking and evolution is a prerequisite to attain a proper estimation of other dependent processes. Although the model can simulate complex patterns in horizontally two-dimensional (2D) configurations, the horizontally one-dimensional (1D) mode is usually sufficient to study most wave evolution processes with efficient modeling time for engineering applications.

Coastal wave transformation reproduced by the SWASH has been thus far extensively validated against laboratory experiments. In this regard, Torres-Freyermuth et al. (2012) reported a good agreement between the model outcomes and the experimental measurements for wave transformation on a fringing reef. As well, Smit et al. (2013 and 2014) compared the model outputs with some experimental observations of random and unidirectional waves on a mild-slope beach, wherein the general success of the model to reproduce the surf zone wave characteristics was verified. Ruju et al. (2014) similarly confirmed the model reliability to simulate the run-up induced by irregular wave breaking on a gentle-slope beach by comparing the model results with laboratory experiment measurements. Moreover, de Bakker et al. (2016b) showed the appropriate capability of the SWASH to represent the IG waves generated by nonlinear triad interactions, using the experimental data recorded by Ruessink et al. (2013). In the same way, Mendes et al. (2018) assessed the impact of bars on energy transfer between IG and wind-waves on a dissipative beach utilizing the SWASH.

In contrast to laboratory validations, comparisons between the model results and field measurements are not very extensive. Moreover, some of these few studies incorporating field validations deduced the underestimation of wave-breaking dissipation and the overestimation of IG wave generation by the default 1D mode of the SWASH (e.g., de Bakker et al., 2014; Lerma et al., 2017). Therefore, the present study aimed to accurately investigate the capability of the 1D mode of SWASH to reproduce the profiles and characteristics of nearshore waves during storm periods. The model results were then compared with in-situ data measured on the Nowshahr beaches, located in the Southern Caspian Sea.

In this study, field measurements and conditions are explained in Section 2, and the numerical governing equations and model setup are reviewed in Section 3, as well as analysis methods are provided in Section 4. The results and their discussions, including the model calibration and the findings of time and frequency domain analyses, are then presented in Section 5, and the study is concluded in the last section.

2. Field study area

The Caspian Sea is the largest lake in the world, enclosed between Azerbaijan, Iran, Kazakhstan, Russia, and Turkmenistan. This inland water body has a 371,000 km^2 area and its freshwater is mostly provided by the Volga, the longest European river. The Caspian Sea is divided into three geographic regions, namely, the Northern, the Middle, and the Southern parts. The oceanic depths of more than 900 m can be found in the Southern Caspian Sea. The Northern and Middle parts are typically frozen within winter. This region is mostly encountering northwesterly strong winds, resulting in various hydrodynamic phenomena dependent on wave transformation on the southern beaches of the Caspian Sea. The negligible tidal range in the Southern part, commonly less than 10 cm, alongside the sandy beaches, provides a suitable environment to study shallow-water wave transformations.

The field data acquisition, including water level variations, was thus accomplished on a straight shore perpendicular transect located in the west of Nowshahr Port on the Southern Caspian Sea (Figure 1a). The study area has a sandy and single-barred beach. The measurement program was accordingly started on March 4, 6:00 p.m., and terminated on March 16, 9:00 a.m., 2014, lasting 13 days. Five pressure sensors and an Acoustic Doppler Current Profiler (ADCP) were deployed on the transect at the stations with depths varying between 4.8 m out of the surf zone till 0.8 m near the shore (Figure 1b). A buoy, installed at the depth of 22.5 m by the Iranian Ports and Maritime Organization, also measured the offshore spectral wave height. However, the data collected at this station were not applicable in the present study since the time series of the water level was not accessible. The water column pressure data were continuously recorded at ST1 and ST2 with a rate of four pieces of data per second. Moreover, the water-level and directional wave data were uninterruptedly measured for 17.07 min per hour by the ADCP at ST6. The pressure data were additionally gathered by pressure transducers at the other three stations with a sampling rate of 1 Hz. Data retrieval was mandatory after two days of measurement at these three stations due to the capacity of the data logger. Data recording was also conducted for three two-day cycles at ST3 and ST4 and one cycle at ST5. More details on instrumentation and measurement conditions are presented in Table 1.

The current profiles were measured using the ADCP at ST6 by averaging the velocity values within 20 minutes for each hour. The recoded current magnitude values were less than 0.1 m/s, indicating that no important event, dependent on current interactions, was expected.

The bathymetric data and beach profile were also gathered and recorded by a single-beam echo sounder at the beginning and end of the field measurement period. No significant bathymetric variation could be pointed out within the field measurement period. Moreover, the processed hydrographic data demonstrated no significant lateral variation and bathymetric event, parallel the shoreline. The recorded profile also has a mild bed with an averaged seaward slope of approximately 0.02. Some complementary details about field measurements can be realized in Mahmoudof et al. (2016).

3. Methods

3.1. Governing equations

Over the last decade, non-hydrostatic models have been increasingly implemented to simulate wave evolution under very different conditions, extended from long tsunami waves in oceanic scales to short wind-waves in coastal applications. The SWASH (Zijlema et al., 2011), as an open-source flow-wave model, is thus capable to simulate the free surface of waters, based on non-hydrostatic pressure distribution. The model can also describe nearshore wave transformations across surf and swash zones as results of nonlinear wave interactions, breaking, and runup at shorelines. The model can generally address the equations in the orthogonal and vertical multi-layered approach

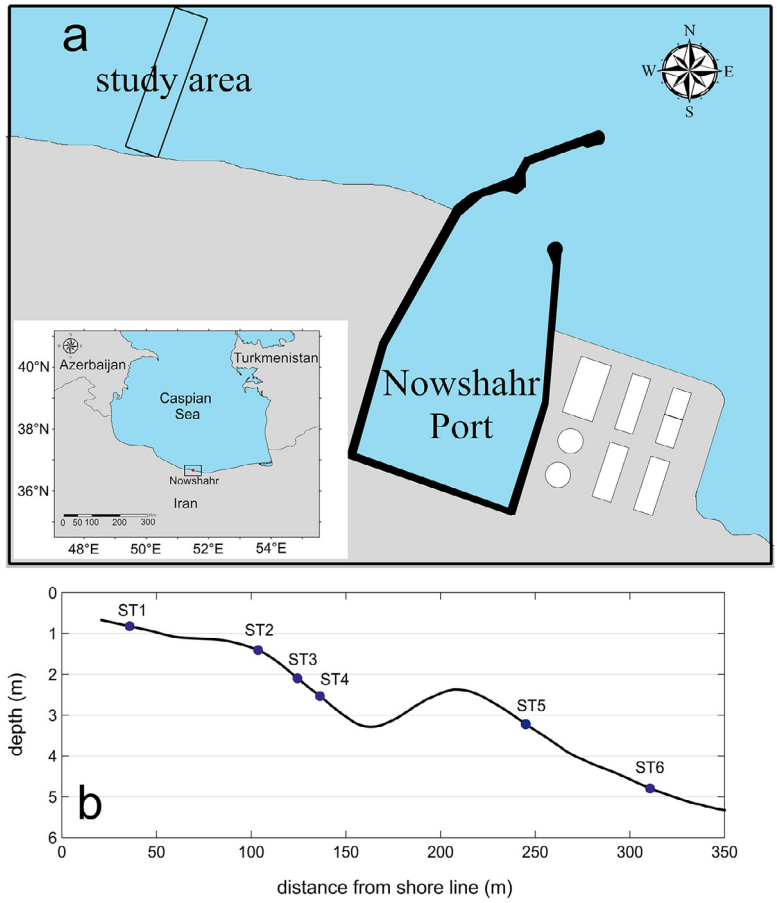

Figure 1 a) Location of the study area; b) bed profile variations of study area and measurement station positions.

Table 1 Characteristics of measurement stations.

Stations	Instrument name	Sampling rate (Hz)	Depth (m)	Distance from shore (m)	Duration
ST1	RBRvirtuoso	4	0.8	35	2014/03/04 – 2014/03/16 (continuously)
ST2	RBRvirtuoso	4	1.4	103	2014/03/04 – 2014/03/16 (continuously)
ST3	DST-centi Star-Oddi	1	2.2	120	2014/03/05 – 2014/03/07, 2014/03/09 – 2014/03/11, 2014/03/12 – 2014/03/14
ST4	DST-centi Star-Oddi	1	2.5	135	2014/03/05 – 2014/03/07, 2014/03/09 – 2014/03/11, 2014/03/12 – 2014/03/14
ST5	DST-centi Star-Oddi	1	3.2	245	2014/03/05 – 2014/03/07
ST6	ADCP	2	4.8	310	2014/03/03 – 2014/03/16 (continuously)

although they are typically introduced in the Cartesian system for simplicity purposes. These governing equations are the Reynolds-Averaged Navier-Stokes (RANS) types for an incompressible and constant-density fluid, which can explain nonlinear shallow-water events. However, the SWASH solves the transformed representation of the following equations in the sigma vertical-layer system:

$$\frac{\partial \eta}{\partial t} + \frac{\partial}{\partial x}\int_{-d}^{\eta} u dz = 0 \tag{1}$$

$$\frac{\partial u}{\partial t} + \frac{\partial uu}{\partial x} + \frac{\partial wu}{\partial z} = -\frac{1}{\rho}\frac{\partial (P_h + P_{nh})}{\partial x} + \frac{\partial \tau_{xz}}{\partial z} + \frac{\partial \tau_{xx}}{\partial x} \tag{2}$$

$$\frac{\partial w}{\partial t}+\frac{\partial uw}{\partial x}+\frac{\partial ww}{\partial z}=-\frac{1}{\rho}\frac{\partial P_{nh}}{\partial z}+\frac{\partial \tau_{zz}}{\partial z}+\frac{\partial \tau_{zx}}{\partial x} \quad (3)$$

$$\frac{\partial u}{\partial x}+\frac{\partial w}{\partial z}=0 \quad (4)$$

where η stands for the free water surface relative to still water level, t denotes the time, d is the still water depth, u and w indicate the depth-averaged flow velocities in the x and z directions, respectively, g shows the gravitational acceleration, ρ represents the fluid density, P_h and P_{nh} are the hydrostatic and non-hydrostatic pressure terms, respectively, and τ parameters are turbulent stresses evaluated based on a turbulent viscosity approximation and applying a standard κ-ε model (e.g., $\tau_{xz} = \nu\partial_z u$, where ν is the kinematic eddy-viscosity).

Near the shores, the main restricting and dissipating factor for wave energy is depth-induced wave breaking, which can exhaust considerable energy content within a few hundred meters. In the SWASH, energy dissipation due to wave breaking is applied by considering the similarity between breaking waves and moving hydraulic jumps along with controlling the vertical speed of the free surface. Accordingly, the wave breaking initiates once this value exceeds a breaking threshold ($\alpha < 1$) of the shallow water celerity as follows:

$$\frac{\partial \eta}{\partial t} > \alpha\sqrt{gh} \quad (5)$$

The wave breaking is also persistent while the fraction coefficient drops to β ($< \alpha$). The default values of α and β coefficients have been respectively set as 0.6 and 0.3 according to Smit et al. (2013), in agreement with Longuet-Higgins and Fox (1977). However, the values of these coefficients depend on the number of vertical layers for each simulation and can be set for a certain vertical layer number. For simulating mild nonlinear waves, propagating from deep to transitional depth, applying one to three layers is often sufficient for the model to capture the wave characteristics in an accurate manner (Smit et al., 2013). In shallow waters, wherein waves are highly nonlinear and close to break and flow velocity gradients increase, higher resolution is necessary for traditional non-hydrostatic models to accurately capture the vertical speed of the free surface. High vertical resolution also increases the time of simulation and reveals the importance of time and accuracy management for modeling purposes. However, the numerical approaches embedded in the SWASH can provide an opportunity to resolve nearshore wave evolution with relatively lower vertical layer numbers (see e.g., Rijnsdrop et al., 2015; Smit et al., 2014). In several studies, different vertical layers have been also applied to assess wave hydrodynamics in the presence of broken waves. In this line, de Bakker et al. (2014), Rijnsdrop et al. (2015), and Lerma et al. (2017) employed two vertical layers, and de Bakker et al. (2016b) and Mendes et al. (2018) set six layers in the vertical direction following Smit et al. (2014).

3.2. Model setup

The present simulation was performed in a non-stationary and 1D mode of the SWASH (version 7.01) using the Cartesian coordinate as the reference framework. It is usually recommended that the numerical spatial resolution should be typically set as 1/100 to 1/50 of the dominant wavelength for flow-wave models to accurately capture wave dynamics (Smit et al., 2013). In the present simulations, the computational grid size was thus selected to be equal to 0.4 m in the 1D mode match to less than 1/150 wavelength, corresponding to the stormy peak period. Therefore, the computational distance with a length of 380 m was divided into 950 separated meshes. This resolution could ensure that at least 30 points were appointed per wavelength for the waves up to $3f_p$ (as three times the main peak frequency) to accurately capture the characteristics of the dominant wavefield. The vertical resolution was additionally defined with six equidistant layers for the model to reproduce the wave evolution in an accurate manner. The time step was also set at $\Delta t = 0.005$ s. The simulation was then repeated for 300 measured bursts for 1200 s. As well, the open boundary was forced by 2048 water level data gathered by the ADCP at ST6 with the rate of 2 Hz. The water level data were also recorded at the locations corresponding to the other five measurement stations. The analyses were accomplished on the most energetic time series with a 1024-s duration for each station and burst. The breaker parameters were regarded as the calibration coefficients to tune the coastal wave energy in the surf zone. Other input parameter values were also set to the default values embedded in the SWASH.

4. Analysis method

In the present study, the SWASH performance to predict the wave transformation in the nearshore shallow water has been investigated qualitatively and quantitatively. Therefore, the time and frequency domain analyses have been accomplished to process the model results and field measurements. The field pressure data were thus converted into water-level ones, applying the depth attenuation-correction method considering the frequency of $f = 0.35$ Hz as the upper correction limit and wind-wave cutoff. The time-domain analysis is founded on zero-down/up crossing analysis. The significant wave height in the time domain analysis ($H_{1/3}$) is defined as the mean of the highest one-third of the waves as follows:

$$H_{1/3}=\frac{1}{N/3}\sum_{j=1}^{N/3}H_j \quad (6)$$

where j represents the rank number of the sorted waves according to their heights in the zero-crossing analysis. The corresponding period parameter to $H_{1/3}$ is also $T_{1/3}$ and calculated as follows:

$$T_{1/3}=\frac{1}{N/3}\sum_{j=1}^{N/3}T_j \quad (7)$$

wherein j is defined as the above and T_j shows the period of waves in the zero-crossing analysis. The parameters of mean height (H_{mean}) and mean period (T_{mean}) of the wave train are also expressed as the average height and period of total waves in a similar approach. It is clear that the number of total counted waves (hereafter referred to as *nw*) is a key factor in the time domain analysis.

For the spectral analysis, all 1024-s time series of water levels, resulting from the measurements and reproduced by the model, were divided into 128-s data blocks with 50% overlap. The coefficients developed from the fast Fourier transform (FFT) were then averaged for each frequency. Therefore, the degree of freedom and fundamental frequency of analysis were approximated as 32 and 0.0078 Hz, respectively.

The frequency of $f = 0.05$ Hz was also regarded as the separation threshold of IG and wind (sea-swell) waves following previous studies (e.g., Herbers et al., 1994, 1995; Thomson et al., 2006). In some researches, the frequency threshold of $f = 0.04$ had been similarly applied for longer oceanic IG waves (e.g., Elgar et al., 1992; Inch et al., 2017; Ruessink, 1998). The heights of IG (H_{ig}) and wind-waves (H_{ss}) were accordingly calculated using the following relationships, respectively:

$$H_{ig} = 4.004\sqrt{\int_0^{0.05\ Hz} E(f)\,df} \tag{8}$$

$$H_{ss} = 4.004\sqrt{\int_{0.05}^{0.35\ Hz} E(f)\,df} \tag{9}$$

where $E(f)$ shows the energy density of wave trains at the frequency of f. Three standard statistical indices of the scatter index (SI), the index of agreement (IA), and the normalized bias (NB) were also utilized to assess the performance and accuracy of the model to reproduce the wave energy content (spectral height; H_{m0}). The predicted and observed values of the wave height (H_{pre} and H_{obs}, respectively) were then placed in the following relationships to calculate the values of the above-mentioned statistical indices.

$$SI = \frac{\sqrt{\frac{1}{N}\sum_{i=1}^{N}\left(H_{pre}^{i} - H_{obs}^{i}\right)^2}}{\bar{H}_{obs}} \tag{10}$$

$$IA = 1.0 - \frac{\sum_{i=1}^{N}\left(H_{pre}^{i} - H_{obs}^{i}\right)^2}{\sum_{i=1}^{N}\left(\left|H_{pre}^{i} - \bar{H}_{obs}\right| + \left|H_{obs}^{i} - \bar{H}_{obs}\right|\right)^2} \tag{11}$$

$$NB = \frac{\sum_{i=1}^{N}\left(H_{pre}^{i} - H_{obs}^{i}\right)}{\sum_{i=1}^{N} H_{obs}^{i}} \tag{12}$$

5. Results and discussion

5.1. Field observations of wave regime

Two storms were the most important events recorded during the field measurements in this study. The wave heights within these two storms also reached approximately 1.3 m (Figure 2). The maximum peak period was more than 9 s and the maximum deviation of mean wave direction from the shore normal direction was 4°. The wave spectra for the storms were composed of one wave system with one single significant peak. As well, the offshore stormy waves had not broken before reaching ST6 according to the observational investigations at the coastal watchtower. The waves of both storms were modest swells, originated from the Middle Caspian Sea near 600 km away from the study area. During the storms, the local wind was also calm with velocities less than 6 m/s, recorded by a coastal synoptic station installed 10 km west of the study area.

Of note, very long-traveling and highly energetic swell waves can't be generally expected in the Caspian Sea due to the absence of a very long fetch, as well frozen body in the Northern part for more than half a year. In the present study, the bursts with the measured wave heights greater than 0.6 m at ST6 (including 19 and 30 bursts within the first and second storms, respectively) were thus supposed as high-energy conditions. The wave breaking was also the dominant shoreward phenomenon for such bursts. Therefore, they were utilized and investigated to tune the depth-induced wave breaking in the SWASH. The directional wave data gathered by the ADCP at ST6 also revealed minor wave reflections from the shoreline. The measured reflection coefficients calculated based on the method explained by Mahmoudof and Azizpour (2020) were less than 8% for the energetic wave conditions.

5.2. Wave energy content calibration

Most nearshore and coastal hydrodynamic processes are controlled by the energy content received from incident waves, directly or indirectly. Therefore, it is necessary to ensure the accuracy of numerical hydrodynamic models in the evaluation of significant spectral wave heights with an emphasis on wave energy. Accordingly, applying an accurate wave-breaking scheme is mandatory for numerical models to appropriately reproduce coastal phenomena.

As mentioned before, the SWASH regards the breaking dissipation for waves with the ratio of vertical speed of free surface to shallow water celerity, varying between β and α ($\beta < \alpha < 1$). The default values of α and β coefficients embedded in the SWASH are also respectively 0.6 and 0.3, according to the modeling results proposed by Smit et al. (2013) with two vertical layers. However, these values have resulted in a significant overestimation of spectral wave heights ($SI = 0.24$, $NB > 0.22$, and $IA < 0.38$) in the present study with the applied model setup within storm periods. This preliminary result indicates that the dissipation of default wave breaking setup is not sufficient for the present 1D mode of the SWASH, in agreement with the findings reported by Lerma et al. (2017). Therefore, considering the breaking parameters as the calibration coefficients was necessary to tune the energy of stormy waves within the studied surf zone. The numerical model was repeated 80 times with different values of α and β in the range of 0.2–0.6 and 0.05–0.30, respectively, with emphasis on pairs incorporating $\alpha < 0.4$ to compensate for the abovementioned overestimation. The statistical indices Eqs. (10)–(12) were then calculated for these 80 tests and three two-dimensional (2D) planes were developed via the Kriging technique (see https://worldwidescience.org/topicpages/k/kriging+interpolation+technique.html for more scientific details) for interpolation and extrapolation. The results are illustrated in Figure 3, wherein the data are shown as black dots in these diagrams. The hollow areas at upper left corners of the diagrams are indicating ranges with $\alpha < \beta$ conditions as theoretically unacceptable values of α and β. All the statistical indices confirm that the coefficients of $\alpha = 0.25$ and $\beta = 0.13$ have resulted in the most accurate reproduction of spectral significant wave height (H_{m0}) during high

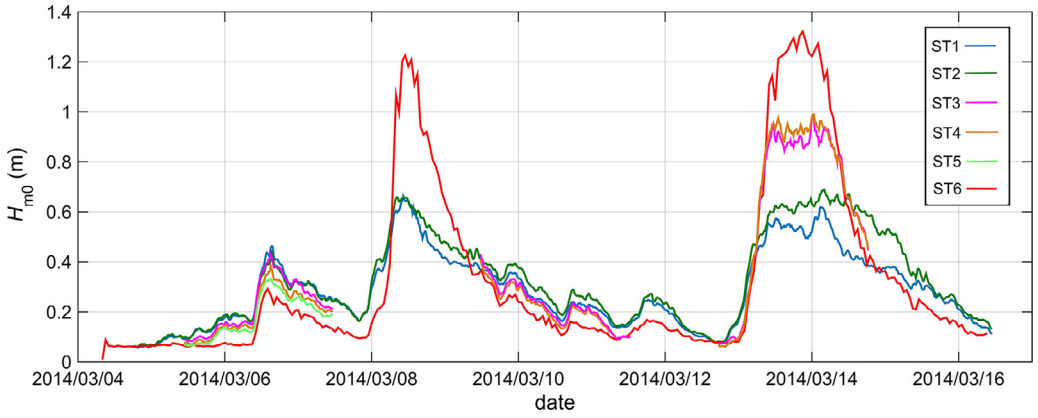

Figure 2 Variations of significant wave heights measured at the six stations within the measurement period.

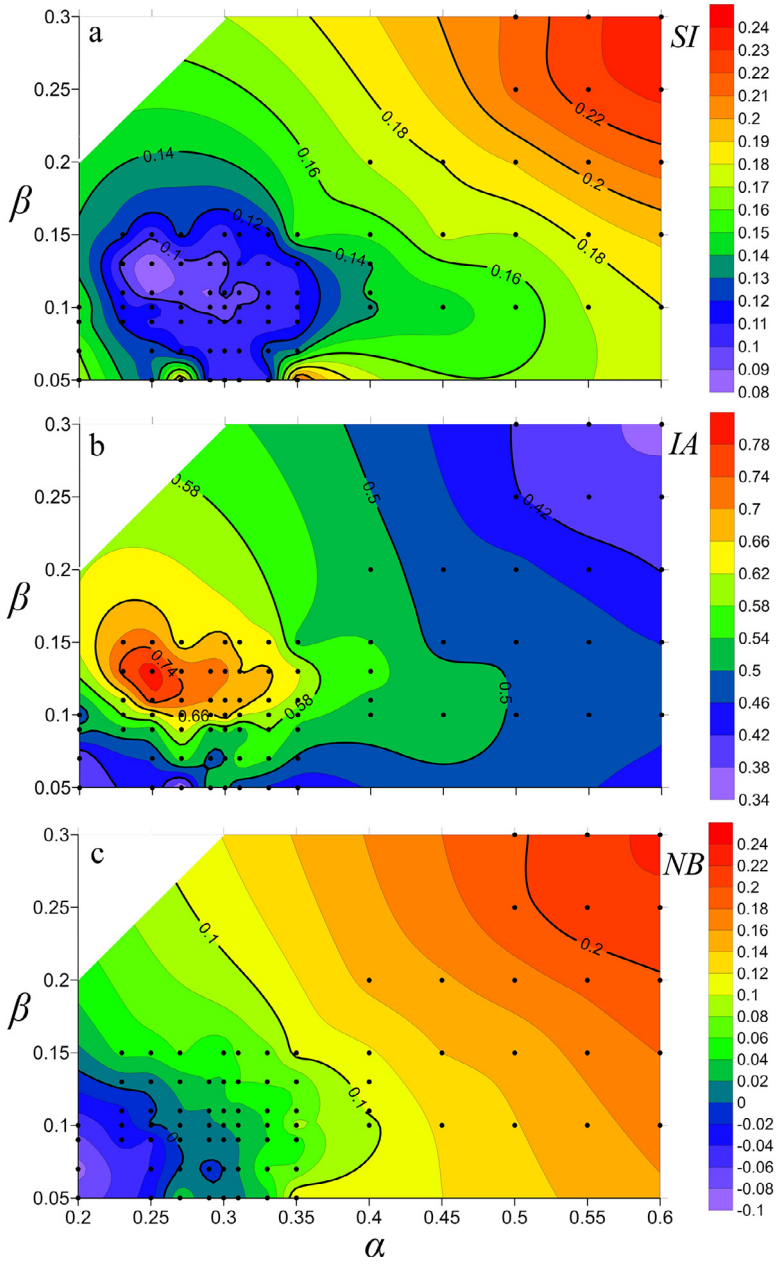

Figure 3 Distribution of statistical indices as functions of α and β; a) *SI*; b) *IA*; and c) *NB*.

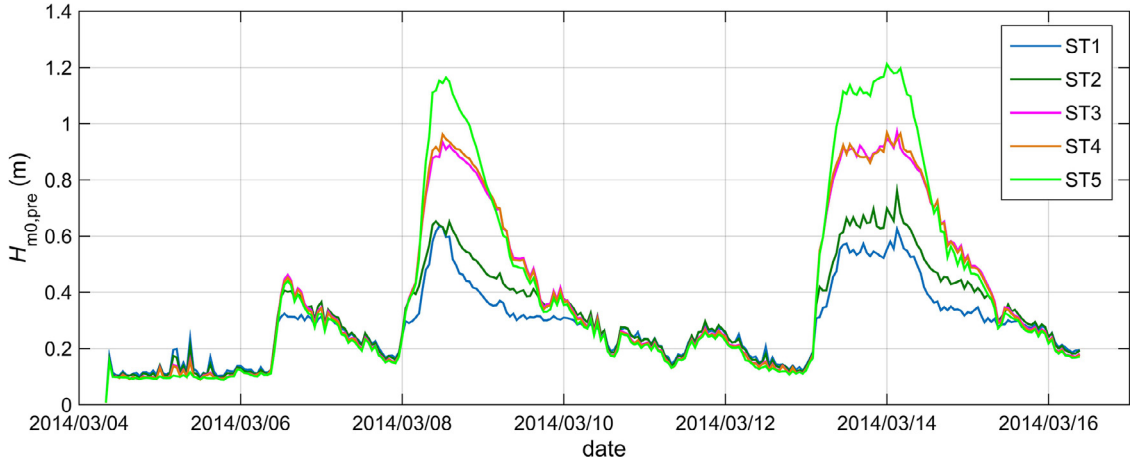

Figure 4 Time series of significant wave height at measurement stations reproduced by SWASH.

energy conditions. For the best result, the attained values of indices were less than 0.08 for the averaged *SI*, more than 0.80 for *IA*, and less than 0.01 for *NB*. The resulted values of breaking coefficients are also in good agreement with those attained in Lerma et al. (2017) for 1D mode and less than those in most of the values found in previous 2D-mode investigations. In this respect, Lerma et al. (2017) found that exerting $\alpha = 0.30$ and $\beta = 0.15$ could significantly improve their 1D model configuration results for very shallow waters. That SWASH calibration was for field-measured data at a complex and ripped bathymetry system. In another recalibration for 2D mode, according to laboratory experimental data, Smit et al. (2014) recommended the values of 1.0 and 0.6 for the coefficients of α and β when using six vertical layers, respectively. Mendes et al. (2018) and de Bakker et al. (2016b) correspondingly followed these suggested values for their laboratory experimental dataset measured by Ruessink et al. (2013). The default values of breaking coefficients were also applied in several 2D studies such as de Bakker et al. (2014), Liang et al. (2015), and Zhang and Stive (2019).

The time series of the spectral wave height (H_{m0}), reproduced by the calibrated model at ST1—ST5, are depicted in Figure 4. Comparing Figure 4 and Figure 2 also reveals a very good capability of the model to accurately predict the variations of energetic wave regime and significant wave heights across the shore. As well, the wave height variations evaluated by the model indicate that the depth-limited condition is dominant during two storm periods and saturated wave breaking decreases the wave height across the shore. Considering the wave setup calculated at the stations (but not shown here) by the model also resulted in relative wave height values (or spectral breaker index, $\gamma = H_{m0}/(d+\text{setup})$) varying in the range of 0.37 at ST5 to 0.66 at ST1. This value at ST1 is comparable to that of 0.73 proposed by Batjjes and Stive (1985) as the constant index for the spectral concept of depth-induced wave breaking.

5.3. Water-level profile assessment

The time-domain variables of $H_{1/3}$, H_{mean}, $T_{1/3}$, T_{mean}, and the *nw* were selected and calculated using the zero-down crossing method to verify the modeled wave profiles. These parameters, particularly period ones and *nw*, are strongly influenced by the variations of short and long waves as the results of wave breaking in the surf zone. The results reveal that the model has properly predicted the general spatial trends of these parameter variations during the storms. For example, the wave height parameters have been expectedly decreased from ST5 to ST1 as the result of depth-induced wave-breaking domination across the shore. On the other hand, the period parameters and *nw* show a shoreward rise and fall, respectively. These variations are the results of shoreward enhancement of IG waves due to water depth attenuation, as reported in several numerical and field studies on different beach environments (e.g., Mahmoudof and Siadatmousavi, 2020; Ruessink, 1998; Thomson et al., 2006).

Figures 5—7 compare the reproduced values of the above-mentioned wave parameters by the model and those observed in the field measurements. It can be generally seen that the *SI* values for height parameters are in the same order at all stations (Figure 5). Since the model has been calibrated for wave energy content, the values of reproduced wave height parameter are expectedly in acceptable accordance with the observed ones. However, the conditions for the period parameters and *nw* are different from the height ones. The resulted period parameters and *nw* by the model are somewhat acceptable at the transitional stations (viz. ST3 and ST4) and inaccurate at the shallow ones (namely, ST1 and ST2). Although the period parameters have been somewhat overestimated at ST3 and ST4, the model has exaggerated these parameters at ST1 and ST2 (Figure 6). While *SI* values for the period parameters are less than 0.15 for transitional stations, similar values have reached more than 1.00 at ST1. In other words, the model has overestimated the period parameters with an increasing trend toward the shore. The model approximately predicted the $T_{1/3}$ values more than two times of observed values at ST1 (the equation of the fitted line in Figure 6a). On the contrary, the model has underestimated *nw* with a shoreward increasing rate of inaccuracy (Figure 7). The predicted rising rate of *nw* values is also about one-quarter of the similar rate measured at the shallowest station (the slope of the fitted line in Figure 7a). All these results imply that a shoreward over-

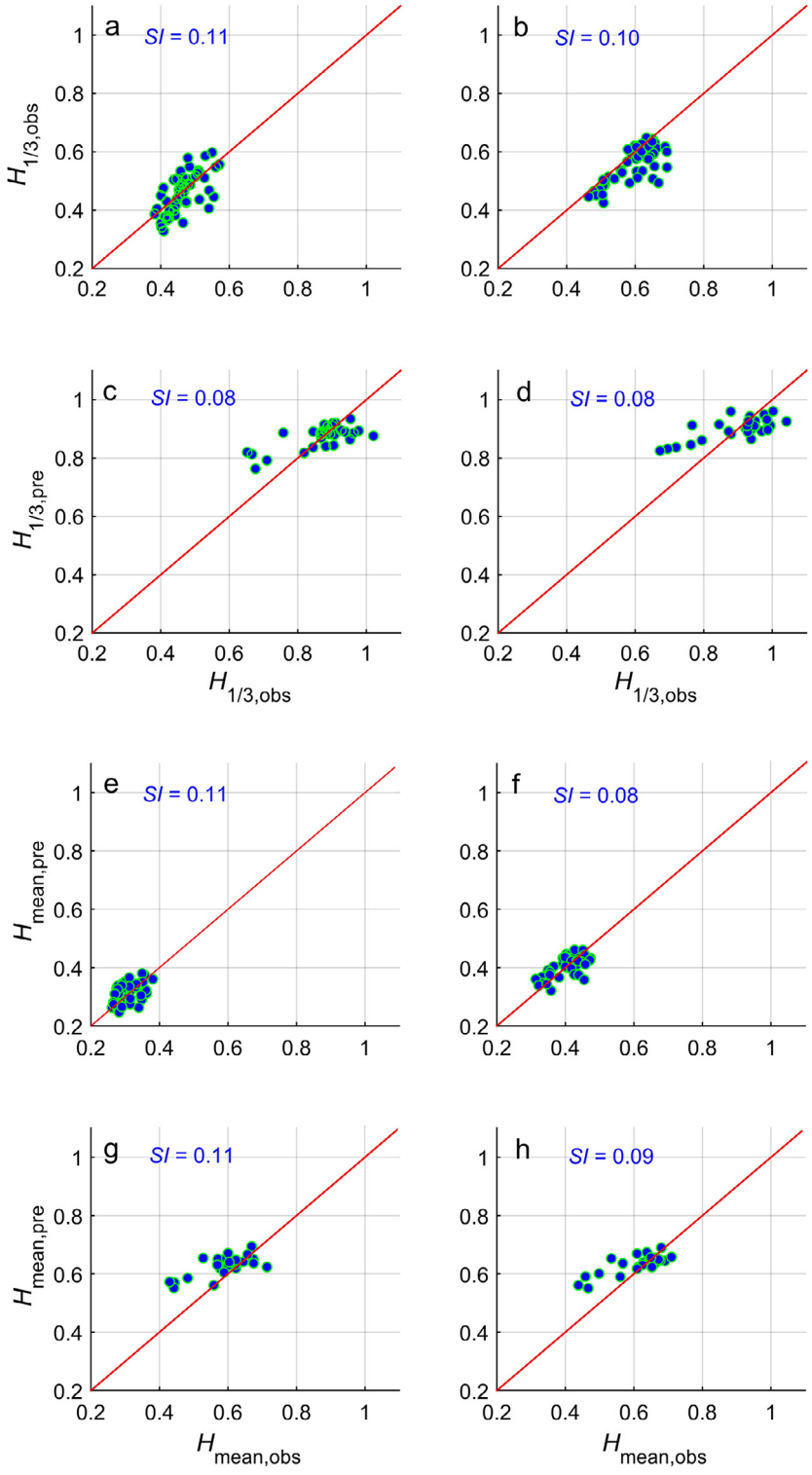

Figure 5 Comparison of height parameters reproduced by the model (pre) and those observed in the field measurements (obs); $H_{1/3}$ at a) ST1; b) ST2; c) ST3; d) ST4 and H_{mean} at e) ST1; f) ST2; g) ST3; h) ST4.

estimation in the generation of long IG waves, as a result of wave breaking or underestimation in short wind-waves can be probably responsible for these inaccurate estimations. High long waves can also make the zero-crossing analysis insensitive to short waves and decrease *nw*, consequently. Moreover, this can normally increase the period parameters.

5.4. Investigation of modeled long and short waves

Typically, the coastal wave regime is influenced by infragravity wave energy within high-energy conditions. These waves rarely break in the surf zone due to their long wavelength. However, breaking is one of their dissipating mech-

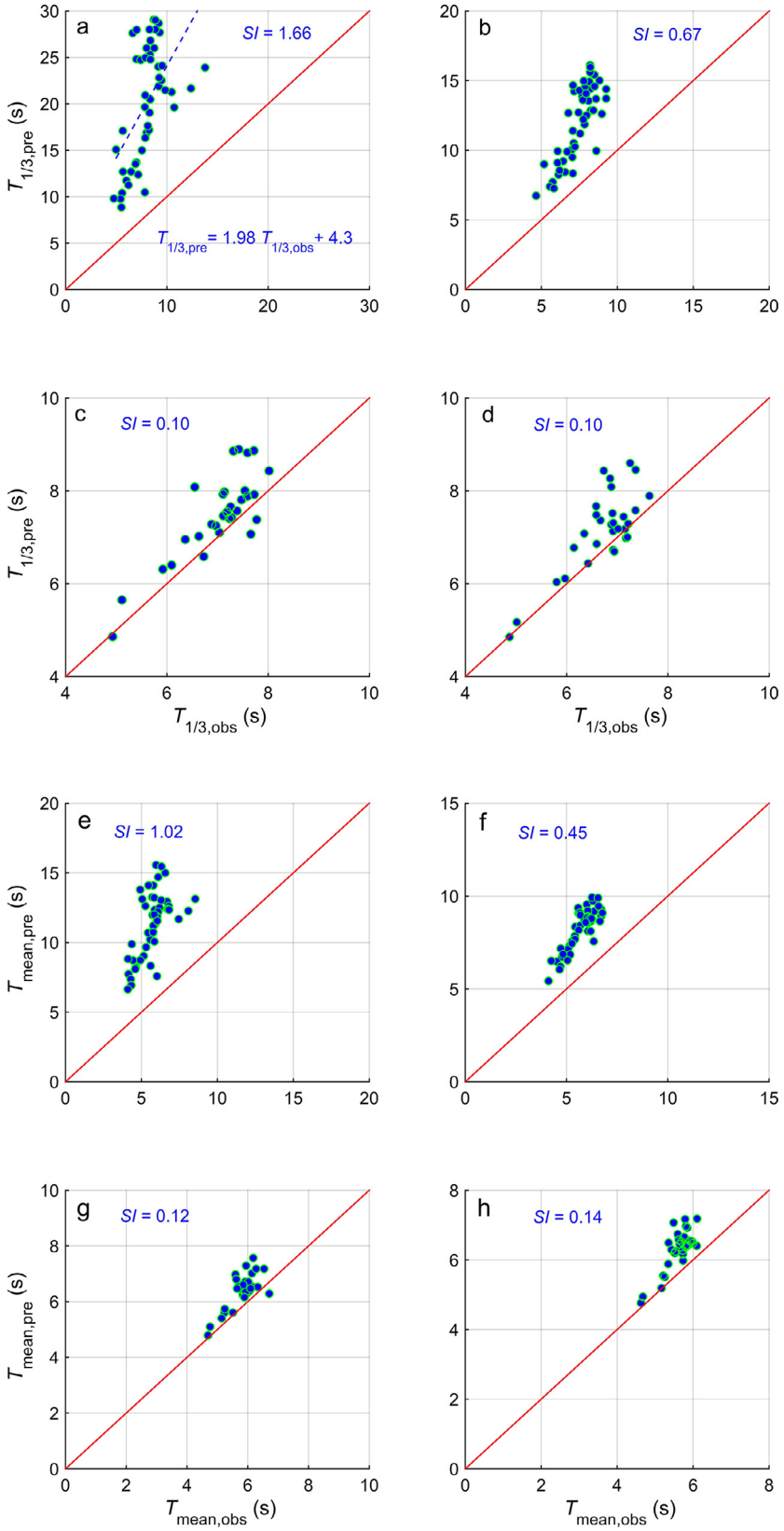

Figure 6 Comparison of period parameters reproduced by the model (pre) and those observed in the field measurements (obs); $T_{1/3}$ at a) ST1; b) ST2; c) ST3; d) ST4 and T_{mean} at e) ST1; f) ST2; g) ST3; h) ST4.

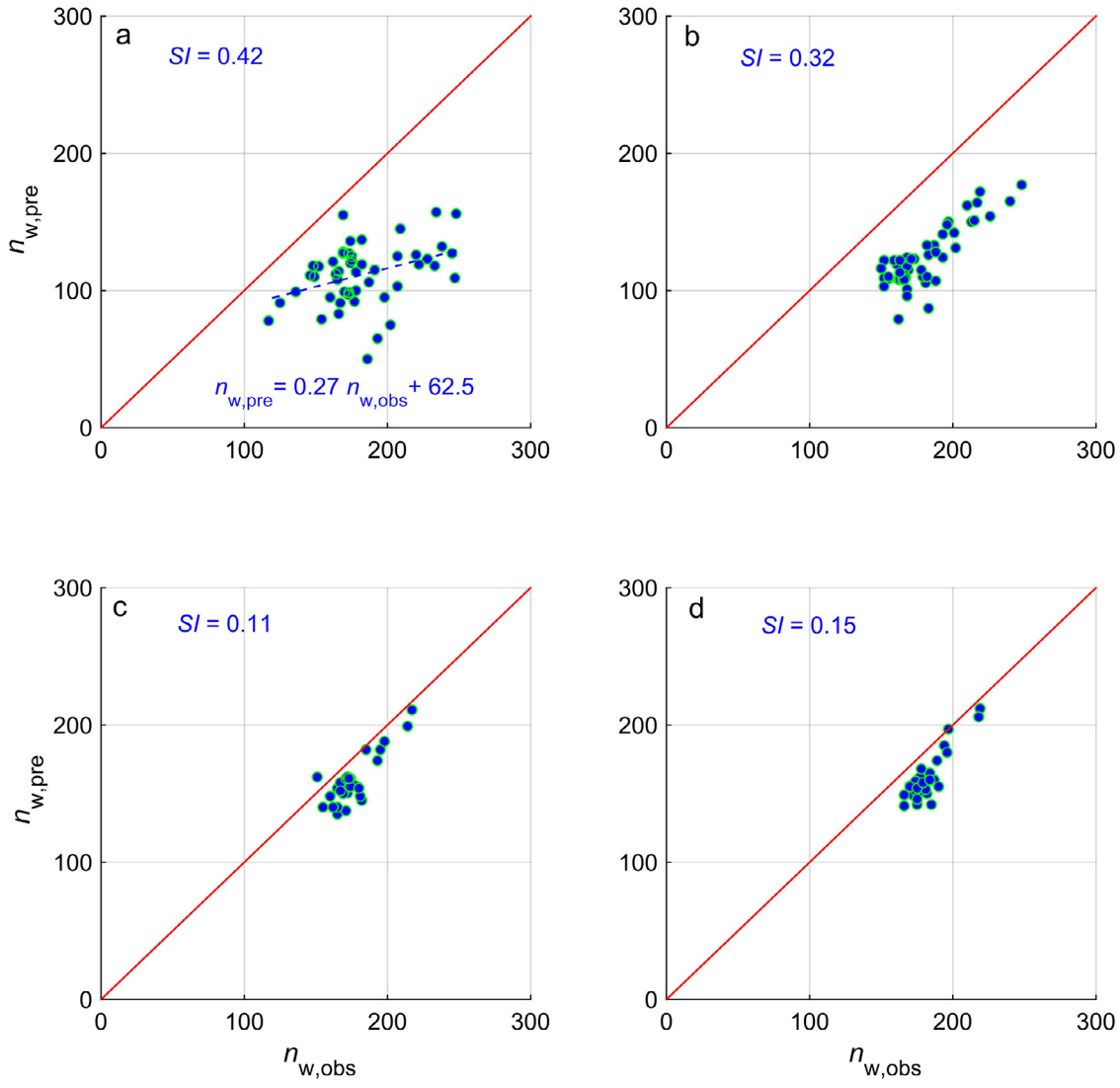

Figure 7 Comparison of the number of waves reproduced by the model (pre) and those observed in the field measurements (obs) at a) ST1; b) ST2; c) ST3; d) ST4.

anisms (de Bakker et al., 2014). Therefore, the increase in wave period parameters is expected at shallow waters within stormy durations. Moreover, wind-wave breaking and decomposition result in bore and short wave generation and some energy transfers to short waves (Mahmoudof, 2018b; Masselink, 1998).

Generally, bispectral analysis is necessary to determine the proportion of released and bound IG waves. However, the IG waves emerging in the present study can be regarded as the released type since they have been generated in the presence of severe breaking of wind-waves, as well all calculated values of β_b are greater than 0.3. The spectral analysis with similar conditions was also performed for model results and field measurements. The heights of IG waves were calculated for all time series using Eq. (8) to assess the accuracy of the model. Figure 8a—d compares the IG wave height values (H_{ig}) reproduced by the model against those observed at all measurement stations for stormy periods. Although the model can appropriately reproduce the saturation of IG waves in very shallow waters, it has considerably overestimated the heights of this type of wave at all stations. Comparing the resulted IG heights at the locations of stations reveals the general capability of the model to show the spatial enhancement of the IG waves. Nevertheless, the slopes of the fitted lines in Figure 8a—d indicates that the relative overestimation has been augmented from the deepest station toward the shore (from ST4 to ST1). Most similar previous studies confirmed the capability of the SWASH to consider the generation and development of released IG waves near shorelines (de Bakker et al., 2016b; Mendes et al., 2018; Rijnsdorp et al., 2015). In contrast, the earlier versions of phase-averaged spectral models such as the Simulating WAves Nearshore (SWAN) or WAVEWATCH III were unable to predict the generation of IG waves as a result of random breaking points of wind-waves. The absence of relevant source-term in those spectral models had made them impractical and fruitless for similar wave modeling in the very shallow water of beaches. Mahmoudof et al. (2018) accordingly tuned the breaking schemes embedded in the SWAN for the wind-waves for the present dataset and inevitably ig-

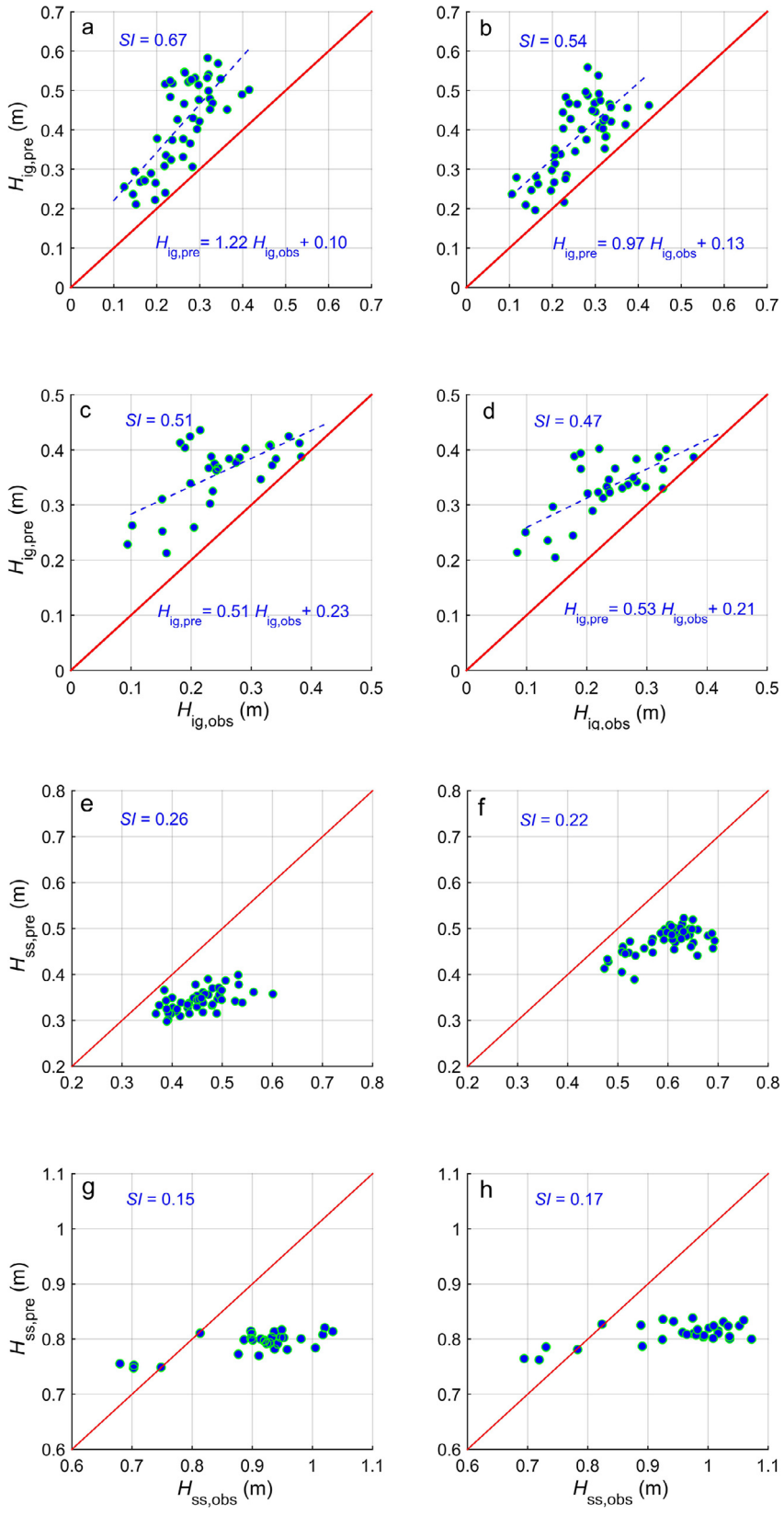

Figure 8 Comparison of infragravity and wind-waves heights reproduced by the model (pre) and those observed in the field measurements (obs); H_{ig} at a) ST1; b) ST2; c) ST3; d) ST4 and H_{ss} at e) ST1; f) ST2; g) ST3; h) ST4.

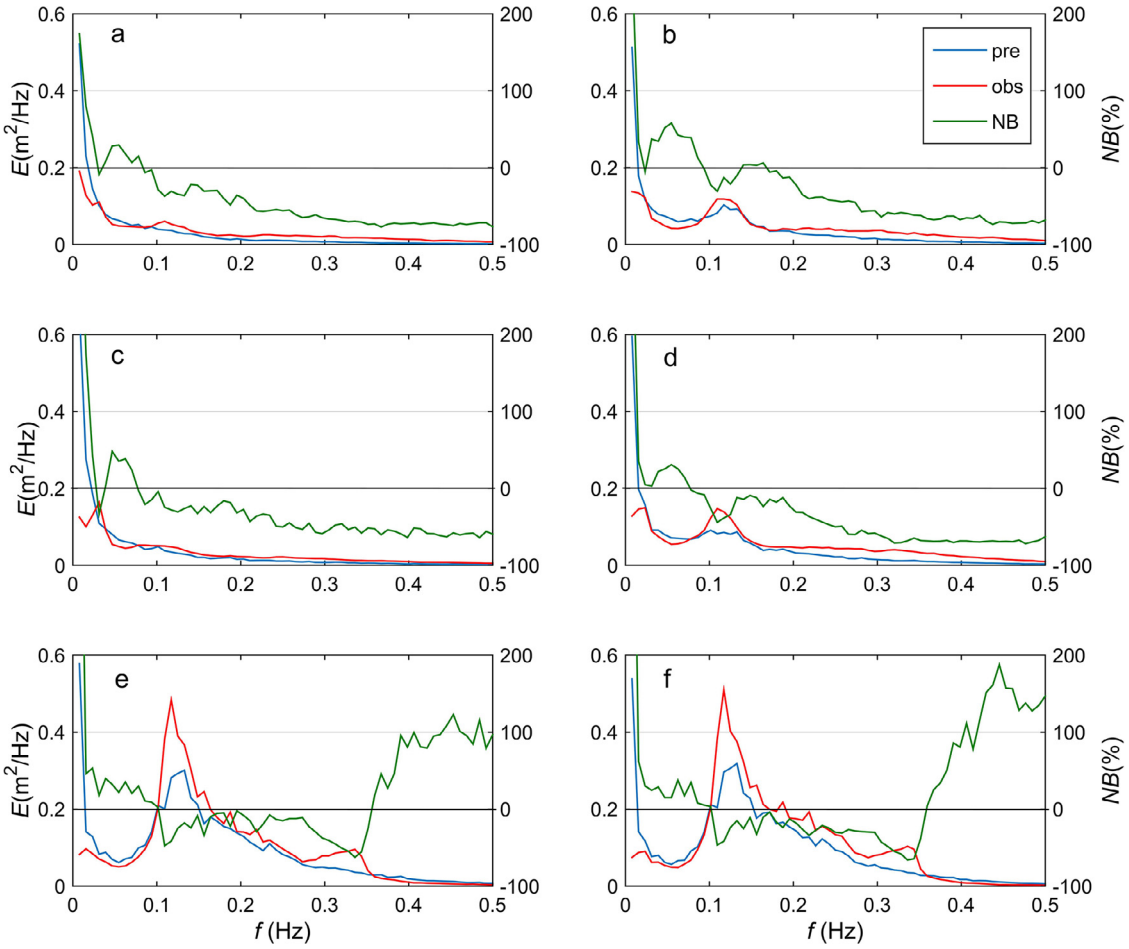

Figure 9 Wave energy and normalized bias spectra for the first storm at: a) ST1; b) ST2; and the second storm at: c) ST1; d) ST2; e) ST3, and f) ST4.

nored the low frequencies less than 0.05 Hz. However, some recent investigations have attempted to equip them with calculations of IG waves, but more verifications and validations are required (Reniers and Zijlema, 2022; Zheng et al., 2021). The study of Ardhuin et al. (2014) was one of the beginner investigations which incorporated the calculations of free IG waves in WAVEWWATCH III. The slope of the fitted curve at ST2 (in Figure 8b) is similar to the results of model run without bottom friction in Ardhuin et al. (2014) at sensor *I* deployed during the DUCK'94 experiment (see Figure 5 in Ardhuin et al., 2014). The slopes of fitted lines in Figure 8c and d are comparable with those of model runs with bottom friction applied only for wind sea and swell waves in that study. However, the comparisons of free IG waves in Ardhuin et al. (2014) pertained to offshore water depths.

A similar assessment was performed for wind-waves ($f > 0.05$ Hz) using Eq. (9) to calculate the relevant heights (H_{ss}). Figure 8e—h shows the results and compares the predicted and measured values of wind-wave heights. It is realized that the model has underestimated the wind-wave heights at all stations. The imperfection has also considerably increased for higher measured waves at ST3 and ST4 (see Figure 8g and h).

For more detailed investigations, the energy spectra were averaged in two groups of model outputs and measurements for the first and second storms with 19- and 30-hour durations, respectively. Also, the normalized bias spectra were evaluated deploying a formulation similar to Eq. (12). The results and comparisons are depicted in the six panels of Figure 9.

Generally, the calibrated model over-dissipated the main spectral peak of the wind-wave at all the stations within both storm durations. Moreover, the energy content of high and low harmonics has been respectively underestimated and overestimated by the model. The negative values of bias spectra are indicating that the wind-wave frequencies between 0.1 and 0.35 Hz have been generally underestimated by the model with a decreasing rate at all stations. On the other hand, the positive normalized bias of model estimation about the energy of low frequencies, $f < 0.1$ Hz, reaches values greater than +200% for $f < 0.02$ Hz. The overestimation in the narrow IG band ($f < 0.05$ Hz) is so important that the predicted energy at the first frequency is more than four times the observed value. Therefore, the first frequency is finally determined as the spectral peak by the model even for transitional depths (ST3 and ST4). Some ignored directional factors in 1D mode can be accordingly responsible for this overestimation. In this regard, de Bakker et al. (2014) pointed out that disregarding directional spreading in the 1D mode could be one of

the probable reasons for the overestimation of IG waves in the model results. Here, the opposite misevaluations of high and low harmonics are approximately balancing together and result in the same total energy content with the field data and equal significant wave heights (H_{m0}) to the measured values. The overestimation of IG and the underestimation of wind-waves have an indirect numerical consequence. These deficiencies result in a decrease in the breaking dissipation rate for the total irregular wave train by further resistance against breaking due to a reduction in wave steepness. Therefore, the lower values of breaking coefficients are necessary to dissipate a certain energy content from longer waves. Consequently, the calibration coefficients found in the present investigation for the 1D mode are less than those recommended in some previous studies for the 2D one. These decreased values of breaking coefficients can accordingly induce over-dissipation for and underestimation of short wind-wave heights. However, the ability of the model to present flattened, double-peaked, and IG-peaked spectra as the result of the frequency transmission of energy at nearshore shallow waters is admirable (Figure 9). However, this transferred energy from the main wind-wave frequencies to lower ones has been overestimated by the model.

In agreement with the measured data, a local peak at the frequency of $f = 0.23$ Hz as two times of the main spectral peak can be found in the model outputs at ST3 and ST4, indicating the probable capability of the model to evaluate and preserve the bound super harmonics (Figure 9e and f). However, these minor local peaks were eliminated after intensifying wave breaking at ST1 and ST2.

An accurate survey in Figure 9 also reveals that some minor challenges may face the model outputs. The minor observed wind-wave (at ~0.11 Hz) and local IG energy peaks (at ~0.03 Hz) are not also represented in the modeled spectrum at ST1 for the first storm (Figure 9a). Similarly, the observed peak frequency is $f = 0.0313$ Hz at ST1 for the second storm, but the model results show the first frequency (fundamental spectral frequency; $f = 0.0078$ Hz) as the calculated peak one (Fig.ure 9c). This means that the model has evaluated longer IG waves than real ones observed at this station. These findings have been similarly repeated at ST2 for both storms (Figure 9b and d).

The investigation of short and long waves reproduced by the model confirms that the calibrated SWASH model can appropriately predict the total energy content of the waves near the shorelines in the study area. However, the modeled water level profiles have some problems, which can be detected using zero-crossing analysis. Such deficiencies are the results of the overestimation of IG energy, the over-dissipation of short wind-waves, and representing lower IG peaks (that is, longer IG waves) by the model than those measured in the study area.

6. Conclusion

The capability of the 1D mode of the SWASH to reproduce the wave profile in very shallow waters was investigated in the present study, and then the results were compared with in-situ data measured at the Southern Caspian Sea during two storm events. The field data included water column pressure variations measured at six stations located on a perpendicular transect of the shoreline in the west of Nowshahr Port within ~two weeks. Two storms, including the modest swell waves with approximately 1.3 m heights, were also the most important recorded events occurring during the measurement period. The bursts with offshore wave heights greater than 0.6 m were then selected to assess the capability of the model to predict the wave evolution across the shore within high-energy conditions.

The model was run in the non-stationary and 1D mode with six vertical layers and spatial resolution less than 1/150 stormy wavelength. Two breaking parameters of the starting (α) and ending (β) wave break were also regarded as the calibration coefficients to tune the wave energy content in the study area. All the statistical indices implemented in the study (*SI, IA, and NB*) agree that the pair values of $\alpha = 0.25$ and $\beta = 0.13$ result in the most accurate values of H_{m0}. The attained values for the statistical parameters were $SI < 0.08$, $IA > 0.80$, and $NB < 0.01$ for the best results. The values of breaking coefficients found in this study are in good agreement with the reported values for the previous 1D mode simulations and less than those for previous similar 2D modeling studies.

The time-domain analysis has shown that although the calibrated model can appropriately predict the wave height parameters ($H_{1/3}$ and H_{mean}), the reproduced water level profiles by the model have some deficiencies. These problems are more significant for shallow stations than transitional water depths. The predicted period parameters ($T_{1/3}$ and T_{mean}) and the number of waves by the model are respectively greater and less than those observed in the field measurements.

Spectral analysis was also applied to investigate the details of the wave energy spectra reproduced by the model. Generally, the capability of the model to transfer energy from wind-waves to IG bands because of time-varying breaking points of wind-waves is satisfactory. However, the model overestimates the IG wave and underestimates the wind-wave energy content with a shoreward increasing rate of inaccuracy. These opposite inaccuracies are closely balanced together and the reproduced spectral wave heights are approximately equal to the observed values. Nevertheless, the modeled energy spectra are different from those observed in the field and then an exaggeration of IG wave heights is resulted from the model. The shoreward inaccuracy is increased in such a way that the fundamental frequency of analysis has been determined as the peak frequency of the nearshore waves by the model. The secondary effect of this inaccuracy is predicting longer IG waves than those determined in the field. Therefore, a more intensive breaking scheme (by exerting low values of breaking coefficients, found in the present study) is required to dissipate a certain energy content from longer waves reproduced by the model.

Finally, higher and longer IG waves and lower wind ones reproduced by the model can make the zero-crossing method insensitive to short wind-waves. Therefore, the time domain analysis represents a lower number of waves and greater values of period parameters for the model results compared with those found in the field measurements.

Acknowledgments

This study was supported by the Iranian National Institute for Oceanography and Atmospheric Science via project number INIOAS-399-021-01-038-01.

References

Ardhuin, F., Rawat, A., Aucan, J., 2014. A numerical model for free infragravity waves: Definition and validation at regional and global scales. Ocean Model. 77, 20—32. https://doi.org/10.1016/j.ocemod.2014.02.006

Battjes, J., Bakkenes, H., Janssen, T., Van Dongeren, A., 2004. Shoaling of subharmonic gravity waves. J. Geophys. Res. - Oceans 109. https://doi.org/10.1029/2003JC001863

Battjes, J., Stive, M., 1985. Calibration and verification of a dissipation model for random breaking waves. J. Geophys. Res. - Oceans (1978—2012) 90, 9159—9167. https://doi.org/10.1029/JC090iC05p09159

de Bakker, A., Brinkkemper, J., Van der Steen, F., Tissier, M., Ruessink, B., 2016a. Cross-shore sand transport by infragravity waves as a function of beach steepness. J. Geophys. Res. F: Earth Surf. 121, 1786—1799. https://doi.org/10.1002/2016JF003878

de Bakker, A., Tissier, M., Ruessink, B., 2014. Shoreline dissipation of infragravity waves. Cont. Shelf Res. 72, 73—82. https://doi.org/10.1016/j.csr.2013.11.013

de Bakker, A., Tissier, M., Ruessink, B., 2016b. Beach steepness effects on nonlinear infragravity-wave interactions: A numerical study. J. Geophys. Res. - Oceans 121, 554—570. https://doi.org/10.1002/2015JC011268

de Vries, J.v.T., Van Gent, M., Walstra, D., Reniers, A., 2008. Analysis of dune erosion processes in large-scale flume experiments. Coast. Eng. 55, 1028—1040. https://doi.org/10.1016/j.coastaleng.2008.04.004

Elgar, S., Herbers, T., Okihiro, M., Oltman-Shay, J., Guza, R., 1992. Observations of infragravity waves. J. Geophys. Res. 97, 15573—15577. https://doi.org/10.1029/92JC01316

Gao, J., Ji, C., Gaidai, O., Liu, Y., Ma, X., 2017. Numerical investigation of transient harbor oscillations induced by N-waves. Coast. Eng. 125, 119—131. https://doi.org/10.1016/j.coastaleng.2017.03.004

Gao, J., Ma, X., Dong, G., Chen, H., Liu, Q., Zang, J., 2021. Investigation on the effects of Bragg reflection on harbor oscillations. Coast. Eng. 170, 103977. https://doi.org/10.1016/j.coastaleng.2021.103977

Gao, J., Ma, X., Zang, J., Dong, G., Ma, X., Zhu, Y., Zhou, L., 2020. Numerical investigation of harbor oscillations induced by focused transient wave groups. Coast. Eng. 158, 103670. https://doi.org/10.1016/j.coastaleng.2020.103670

Gao, J., Zhou, X., Zhou, L., Zang, J., Chen, H., 2019. Numerical investigation on effects of fringing reefs on low-frequency oscillations within a harbor. Ocean Eng. 172, 86—95. https://doi.org/10.1016/j.oceaneng.2018.11.048

González-Marco, D., Sierra, J.P., de Ybarra, O.F., Sánchez-Arcilla, A., 2008. Implications of long waves in harbor management: the Gijón port case study. Ocean Coast. Manage. 51, 180—201. https://doi.org/10.1016/j.ocecoaman.2007.04.001

Guza, R., Thornton, E.B., 1985. Observations of surf beat. J. Geophys. Res. - Oceans 90, 3161—3172. https://doi.org/10.1029/JC090iC02p03161

Guza, R.T., Thornton, E.B., 1982. Swash oscillations on a natural beach. J. Geophys. Res. - Oceans 87, 483—491. https://doi.org/10.1029/JC087iC01p00483

Hasselmann, K., 1962. On the non-linear energy transfer in a gravity-wave spectrum Part 1. General theory. J. Fluid Mech. 12, 481—500. https://doi.org/10.1017/S0022112062000373

Herbers, T., Elgar, S., Guza, R., 1994. Infragravity-frequency (0.005—0.05 Hz) motions on the shelf. Part I: Forced Waves. J. Phys. Oceanogr. 24 (5), 917—927. https://doi.org/10.1175/1520-0485(1994)024<0917:IFHMOT>2.0.CO;2

Herbers, T., Elgar, S., Guza, R., O'Reilly, W., 1995. Infragravity-frequency (0.005—0.05 Hz) motions on the shelf. Part II: Free waves. J. Phys. Oceanogr. 25 (6), 1063—1079. https://doi.org/10.1175/1520-0485(1995)025<1063:IFHMOT>2.0.CO;2

Hoefel, F., Elgar, S., 2003. Wave-induced sediment transport and sandbar migration. Science 299, 1885—1887. https://doi.org/10.1126/science.1081448

Inch, K., Davidson, M., Masselink, G., Russell, P., 2017. Observations of nearshore infragravity wave dynamics under high energy swell and wind-wave conditions. Cont. Shelf Res. 138, 19—31. https://doi.org/10.1016/j.csr.2017.02.010

Komen, G., Cavaleri, L., Donelan, M., Hasselmann, K., Hasselmann, S., Janssen, P., 1994. Dynamics and Modelling of Ocean Waves Cambridge University Press, 532 pp. https://doi.org/10.1017/CBO9780511628955

Lerma, A.N., Pedreros, R., Robinet, A., Sénéchal, N., 2017. Simulating wave setup and runup during storm conditions on a complex barred beach. Coast. Eng. 123, 29—41. https://doi.org/10.1016/j.coastaleng.2017.01.011

Liang, B., Wu, G., Liu, F., Fan, H., Li, H., 2015. Numerical study of wave transmission over double submerged breakwaters using non-hydrostatic wave model. Oceanologia 57 (4), 308—317. https://doi.org/10.1016/j.oceano.2015.07.002

Longuet-Higgins, M., Fox, M., 1977. Theory of the almost-highest wave: the inner solution. J. Fluid Mech. 80, 721—741. https://doi.org/10.1017/S0022112077002444

Longuet-Higgins, M.S., Stewart, R., 1962. Radiation stress and mass transport in gravity waves, with application to 'surf beats. J. Fluid Mech. 13, 481—504. https://doi.org/10.1017/S0022112062000877

Longuet-Higgins, M.S., Stewart, R., 1964. Radiation stresses in water waves; a physical discussion, with applications. Deep Sea Res. Oceanogr. Abstr. Elsevier, 529—562. https://doi.org/10.1016/0011-7471(64)90001-4.

Longuet-Higgins, M.S., 1970. Longshore currents generated by obliquely incident sea waves: 1. J. Geophys. Res. 75, 6778—6789. https://doi.org/10.1029/JC075i033p06778

Ma, G., Shi, F., Kirby, J.T., 2012. Shock-capturing non-hydrostatic model for fully dispersive surface wave processes. Ocean Model. 43, 22—35. https://doi.org/10.1016/j.ocemod.2011.12.002

MacMahan, J.H., Thornton, E.B., Reniers, A.J., 2006. Rip current review. Coastal Eng. 53, 191—208. https://doi.org/10.1016/j.coastaleng.2005.10.009

Madsen, P.A., Bingham, H., Liu, H., 2002. A new Boussinesq method for fully nonlinear waves from shallow to deep water. J. Fluid Mech. 462, 1—30. https://doi.org/10.1017/S0022112002008467

Mahmoudof, S.M., 2018a. Investigation of Infragravity Waves Dependency on Wind Waves for Breaking and Nonbreaking Conditions in the Sandy Beaches of Southern Caspian Sea (Nowshahr Port). Int. J. Coastal Offsh. Eng. 1, 13—20. https://doi.org/10.29252/ijcoe.1.4.13

Mahmoudof, M., 2018b. Study of Low and High Harmonic Energy Amplification Due to Outer Surf-zone Wave Breaking. J. Oceanogr. 9, 1—9. https://doi.org/10.29252/joc.9.34.1

Mahmoudof, S.M., Azizpour, J., 2020. Field observation of wave reflection from plunging cliff coasts of Chabahar. App. Ocean Res. 95, 102029. https://doi.org/10.1016/j.apor.2019.102029

Mahmoudof, S.M., Azizpour, J., Eyhavand-Koohzadi, A., 2021. Observation of infragravity wave processes near the coastal cliffs

of Chabahar (Gulf of Oman). Estuarine Coast. Shelf Sci. 107226. https://doi.org/10.1016/j.ecss.2021.107226
Mahmoudof, S.M., Badiei, P., Siadatmousavi, S.M., Chegini, V., 2016. Observing and estimating of intensive triad interaction occurrence in very shallow water. Cont. Shelf Res. 122, 68—76. https://doi.org/10.1016/j.csr.2016.04.003
Mahmoudof, S.M., Badiei, P., Siadatmousavi, S.M., Chegini, V., 2018. Spectral Wave Modeling in Very Shallow Water at Southern Coast of Caspian Sea. J. Marine Sci. App. 17, 140—151. https://doi.org/10.1007/s11804-018-0011-y
Mahmoudof, S.M., Siadatmousavi, S.M., 2020. Bound infragravity wave observations at the Nowshahr beaches, southern Caspian Sea. App. Ocean Res. 98, 102122. https://doi.org/10.1016/j.apor.2020.102122
Masselink, G., 1998. Field investigation of wave propagation over a bar and the consequent generation of secondary waves. Coast. Eng. 33, 1—9. https://doi.org/10.1016/s0378-3839(97)00032-x
Mendes, D., Pinto, J.P., Pires-Silva, A.A., Fortunato, A.B., 2018. Infragravity wave energy changes on a dissipative barred beach: A numerical study. Coast. Eng. 140, 136—146. https://doi.org/10.1016/j.coastaleng.2018.07.005
Nwogu, O., 1993. Alternative form of Boussinesq equations for nearshore wave propagation. J. Waterw. Port C. 119, 618—638. https://doi.org/10.1061/(ASCE)0733-950X
Reniers, A., Zijlema, M., 2022. SWAN SurfBeat-1D. Coast. Eng. 172, 104068. https://doi.org/10.1016/j.coastaleng.2021.104068
Rijnsdorp, D.P., Ruessink, G., Zijlema, M., 2015. Infragravity-wave dynamics in a barred coastal region, a numerical study. J. Geophys. Res. - Oceans 120, 4068—4089. https://doi.org/10.1002/2014JC010450
Roelvink, D., Reniers, A., Van Dongeren, A., de Vries, J.v.T., McCall, R., Lescinski, J., 2009. Modelling storm impacts on beaches, dunes and barrier islands. Coast. Eng. 56, 1133—1152. https://doi.org/10.1016/j.coastaleng.2009.08.006
Ruessink, B., 1998. The temporal and spatial variability of infragravity energy in a barred nearshore zone. Cont. Shelf Res. 18, 585—605. https://doi.org/10.1016/S0278-4343(97)00055-1
Ruessink, B.G., Michallet, H., Bonneton, P., Mouazé, D., Lara, J., Silva, P.A., Wellens, P., 2013. Globex: wave dynamics on a gently sloping laboraty beach. Proc. Coast. Dyn. 2013, 1351—1362.
Ruju, A., Lara, J.L., Losada, I.J., 2012. Radiation stress and low-frequency energy balance within the surf zone: A numerical approach. Coast. Eng. 68, 44—55. https://doi.org/10.1016/j.coastaleng.2012.05.003
Ruju, A., Lara, J.L., Losada, I.J., 2014. Numerical analysis of run-up oscillations under dissipative conditions. Coast. Eng. 86, 45—56. https://doi.org/10.1016/j.coastaleng.2014.01.010
Sheremet, A., Guza, R., Elgar, S., Herbers, T., 2002. Observations of nearshore infragravity waves: Seaward and shoreward propagating components. J. Geophys. Res. - Oceans 107. https://doi.org/10.1029/2001JC000970
Smit, P., Janssen, T., Holthuijsen, L., Smith, J., 2014. Non-hydrostatic modeling of surf zone wave dynamics. Coastal Eng. 83, 36—48. https://doi.org/10.1016/j.coastaleng.2013.09.005
Smit, P., Zijlema, M., Stelling, G., 2013. Depth-induced wave breaking in a non-hydrostatic, near-shore wave model. Coastal Eng 76, 1—16. https://doi.org/10.1016/j.coastaleng.2013.01.008
Stelling, G., Zijlema, M., 2003. An accurate and efficient finite-difference algorithm for non-hydrostatic free-surface flow with application to wave propagation. Int. J. Numer. Methods Fluids 43, 1—23. https://doi.org/10.1002/fld.595
Svendsen, I.A., 1984. Mass flux and undertow in a surf zone. Coast. Eng. 8, 347—365. https://doi.org/10.1016/0378-3839(84)90030-9
Symonds, G., Huntley, D.A., Bowen, A.J., 1982. Two-dimensional surf beat: Long wave generation by a time-varying breakpoint. J. Geophys. Res. - Oceans 87, 492—498. https://doi.org/10.1029/JC087iC01p00492
The Wamdi Group, 1988. The WAM model-a third generation ocean wave prediction model. J. Phys. Oceanogr. 18, 1775—1810. https://doi.org/10.1175/1520-0485
Thomson, J., Elgar, S., Raubenheimer, B., Herbers, T., Guza, R., 2006. Tidal modulation of infragravity waves via nonlinear energy losses in the surfzone. Geophys. Res. Lett. 33. https://doi.org/10.1029/2005GL025514
Torres-Freyermuth, A., Mariño-Tapia, I., Coronado, C., Salles, P., Medellín, G., Pedrozo-Acuña, A., Silva, R., Candela, J., Iglesias-Prieto, R., 2012. Wave-induced extreme water levels in the Puerto Morelos fringing reef lagoon. Nat. Hazard. Earth Sys. 12, 3765—3773. https://doi.org/10.5194/nhess-12-3765-2012
Torres-Freyermuth, A., Losada, I.J., Lara, J.L., 2007. Modeling of surf zone processes on a natural beach using Reynolds-Averaged Navier-Stokes equations. J. Geophys. Res. - Oceans 112. https://doi.org/10.1029/2006JC004050
Webb, S.C., Zhang, X., Crawford, W., 1991. Infragravity waves in the deep ocean. J. Geophys. Res. - Oceans 96, 2723—2736. https://doi.org/10.1029/90JC02212
Wei, G., Kirby, J.T., Grilli, S.T., Subramanya, R., 1995. A fully nonlinear Boussinesq model for surface waves. Part 1. Highly nonlinear unsteady waves. J. Fluid Mech. 294, 71—92. https://doi.org/10.1017/S0022112095002813
Yamazaki, Y., Kowalik, Z., Cheung, K.F., 2009. Depth-integrated, non-hydrostatic model for wave breaking and run-up. Int. J. Numer. Method. Fluids 61, 473—497. https://doi.org/10.1002/fld.1952
Zhang, R., Stive, M.J., 2019. Numerical modelling of hydrodynamics of permeable pile groins using SWASH. Coast. Eng. 153, 103558. https://doi.org/10.1016/j.coastaleng.2019.103558
Zheng, Z., Ma, X., Ma, Y., Huang, X., Dong, G., 2021. Modeling of coastal infragravity waves using the spectral model WAVEWATCH III. Coast. Eng. 170, 104016. https://doi.org/10.1016/j.coastaleng.2021.104016
Zijlema, M., Stelling, G., Smit, P., 2011. SWASH: An operational public domain code for simulating wave fields and rapidly varied flows in coastal waters. Coast. Eng. 58, 992—1012. https://doi.org/10.1016/j.coastaleng.2011.05.015